**Supplementary Information**

# Molecularly Crowded Water-in-Salt Electrolyte enabled All climate operational high voltage flexible $MnO_2$ supercapacitor

Prahlada Thippeswamy,[1] Vinay Arya, [2] Indranil Dey,[3] Chirodeep Bakli, [2]* Debasis Ghosh[1]*

[1]*Centre for Nano and Material Sciences, JAIN (Deemed to be University), Kanakapura Road, Bangalore, Karnataka, 562112 India*

[2]*Thermofluidics and Nanotechnology for Sustainable Energy Systems Laboratory, School of Energy Science and Engineering, Indian Institute of Technology Kharagpur, Kharagpur, West Bengal, 721302 India*

[3]*Department of Materials Engineering, Indian Institute of Science, Bengaluru, 560012, India*

***Corresponding author:***

*Debasis Ghosh (g.debasis@jainuniversity.ac.in ; debasisghosh88@gmail.com)*

*Chirodeep Bakli (chirodeep@iitkgp.ac.in)*

## Experimental Section:

### Synthesis of Laser-Induced graphene (LIG):

Laser induced graphene was fabricated using a commercial $CO_2$ laser engraving machine (Han's Yueming, Model: CMA0604BA, 25W). Polyimide sheets (procured from McMaster-Carr) served as substrate onto which $CO_2$ laser was patterned to produce LIG. The laser parameters were carefully optimized, employing a power setting of 13%, a scan speed of 18 mm/s, and resolution of 1270 DPI to achieve precise and uniform scribing.

Interdigitated patterns were designed with individual electrode fingers having a width of 0.7 mm and a fixed length of 1.5 cm. The inter-finger spacing was maintained at 0.7 mm. To ensure complete carbonization and a well-developed porous carbon, three consecutive laser scribing cycles were performed on each pattern.

**Electrodeposition of $MnO_2$ and Fabrication of symmetric pseudocapacitor:**

The $MnO_2$ was electrodeposited onto the interdigital pattern LIG in a three-electrode setup. The LIG served as working electrode, with a platinum wire as counter electrode and saturated calomel electrode as the reference electrode. Electrodeposition was performed using an aqueous solution containing 0.1 M $Mn(Ac)_2$ and 0.1 M $Na_2SO_4$. A constant voltage of 1 V was applied for 5 minutes at room temperature. After the deposition the materials were washed carefully with excess DI water and dried at 60° C for 12 hours. The active mass loading of electrodeposited $MnO_2$ on LIG is $0.67 \pm 0.03$ mg/cm$^2$ per electrode. The average thickness of the $MnO_2$ layer is 74 μm, corresponding to a packing density of approximately $90.1 \pm 4.3$ mg/cm$^3$. The $MnO_2$ was electrodeposited onto the whole area of the LIG to fabricate LIG supported $MnO_2$ symmetric supercapacitor ($MnO_2$-SSC) with planer electrode architecture. The $MnO_2$-SSC was tested in a 17 m $NaClO_4$ in water and ethylene glycol mixture (1:2 V/V) electrolyte.

**Electrochemical characterizations:** The fabricated device was tested within a potential window of 0-2.5V via cyclic voltammetry, galvanostatic charge discharge and electrochemical impedance spectroscopy study. For the cycle stability study at low/room temperature, the 4 min electrodeposited cell was used.

**Simulation Details:**

For baseline electrolyte simulations, we construct a simulation domain with water, sodium ions, and chlorate ions. To understand the effect of the electrode, we prepare a 4x4 unit cell structure of $MnO_2$ and fix it in the middle of the domain. We then pack the system similarly using PACKMOL. The effect of ethylene glycol is considered for both configurations to assess its influence on the system behavior.

Following initial structure generation, we perform energy minimization to remove any bad contacts between atoms that may arise due to the packing. Once this is achieved, we perform isobaric-isothermal (NPT) simulations for 1000 picoseconds at a step size of 0.1 femtoseconds to accurately capture the dynamics of the phenomenon. The pressure is controlled using a Berendsen barostat at 1 atm, and the temperature is controlled using a Nose-Hoover thermostat at 300 K.[1] The cut-off radius is kept at 1 nm. All simulations are performed using the open-source GROMACS software, and visualization is done with the VMD software.[2, 3]

**List of simulations:**

**A. Interactions of Electrolyte System**

| | **Water** | **Na** | **$ClO_4$** |
|---|---|---|---|
| 1m | 3500 | 63 | 63 |
| 6m | 3500 | 378 | 378 |
| 12m | 3500 | 757 | 757 |
| 17m | 3500 | 1072 | 1072 |

**B. Effect of EG on Electrolyte:**

| | **Water** | **Na** | **$ClO_4$** | **EG** |
|---|---|---|---|---|
| 0 | 3500 | 1072 | 1072 | 0 |
| 0.3 | 3500 | 1072 | 1072 | 305 |
| 0.5 | 3500 | 1072 | 1072 | 508 |
| 0.8 | 3500 | 1072 | 1072 | 813 |
| 1.2 | 3500 | 1072 | 1072 | 1219 |
| 1.6 | 3500 | 1072 | 1072 | 1625 |
| 2 | 3500 | 1072 | 1072 | 2032 |

**C. Interactions with Electrode material (only electrolyte):**

| | **Water** | **Na** | **$ClO_4$** | **EG** | **$MnO_2$ sheets** |
|---|---|---|---|---|---|
| 1m | 3500 | 63 | 63 | 0 | 1 |

| | | | | | |
|---|---|---|---|---|---|
| 6m | 3500 | 378 | 378 | 0 | 1 |
| 12m | 3500 | 757 | 757 | 0 | 1 |
| 17m | 3500 | 1072 | 1072 | 0 | 1 |

**D. Interactions of electrode with EG and electrolyte:**

| | **Water** | **Na** | **$ClO_4$** | **EG** | **$MnO_2$ sheets** |
|---|---|---|---|---|---|
| 0 | 3500 | 1072 | 1072 | 0 | 1 |
| 0.3 | 3500 | 1072 | 1072 | 305 | 1 |
| 0.5 | 3500 | 1072 | 1072 | 508 | 1 |
| 0.8 | 3500 | 1072 | 1072 | 813 | 1 |
| 1.2 | 3500 | 1072 | 1072 | 1219 | 1 |
| 1.6 | 3500 | 1072 | 1072 | 1625 | 1 |
| 2 | 3500 | 1072 | 1072 | 2032 | 1 |

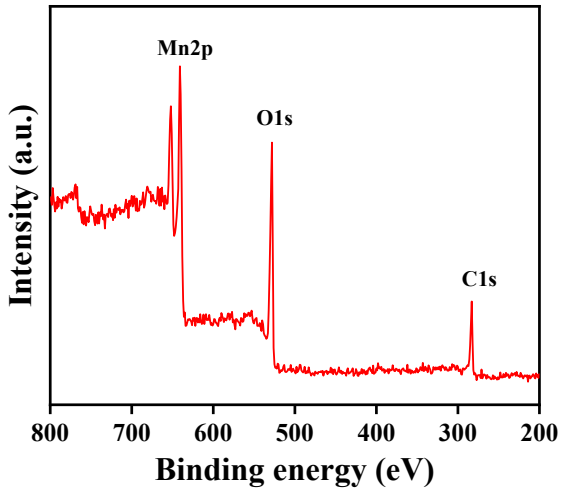


**Figure S1**: XPS survey spectra of electrodeposited $MnO_2$ onto LIG

## Physical properties of the MC-WiSE electrolyte

### Ionic conductivity:

The ionic conductivity of the MC-WiSE electrolyte across different temperatures were determined via EIS analysis in a symmetric cell across different temperatures of -40ºC, RT and 60 ºC. The conductivity was calculated from the equation:

$$\sigma = \frac{L}{R_b \times A}$$

Where $\sigma$ is the ionic conductivity, L is the distance between two electrodes, $R_b$ is the bulk resistance and A is the contact area. The ionic conductivity of the MC-WiSE was determined to be 2.1, 2.7, 7.1 mS/cm at different temperatures of -40ºC, RT and 60 ºC, respectively. Nevertheless, these values were significantly lower than the ionic conductivity measured by Haana conductivity meter, which showed a room temperature ionic conductivity of ~23 mS/cm which increased to 32 mS/cm at 60 °C, representing a ~39% enhancement. We believe, EIS measurements using a two-electrode configuration yielded lower values due to additional contributions from interfacial resistance and geometric uncertainties, which are commonly observed in liquid systems.

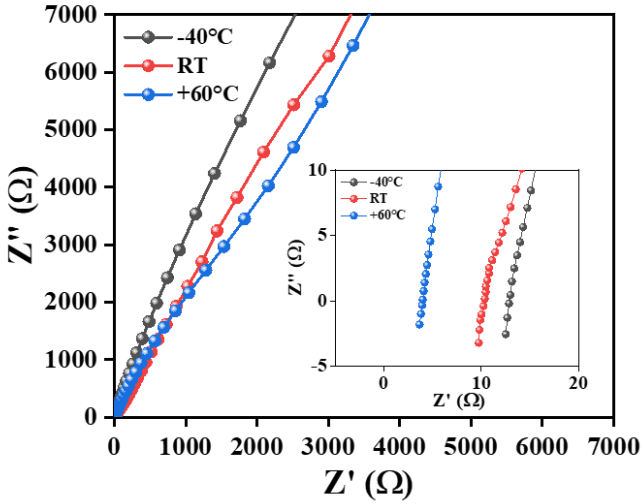


**Figure S2:** EIS analysis of symmetric cell with stainless steel electrodes and MC-WiSE electrolyte at different temperatures

### Room temperature Viscosity:

Rheological measurements, including complex viscosity (η*), were performed using a TA Instruments Discovery HR-3 hybrid rheometer equipped with a Peltier-controlled steel plate and a 40 mm diameter, 1.011° cone-and-plate geometry. Oscillatory frequency sweep tests were conducted for MC-WiSE and 17 m NaClO4 samples at a constant shear strain of 0.1% within the linear viscoelastic region, while the angular frequency was varied from 1 to 10 rad $s^{-1}$. All measurements were carried out at 25 °C. Rheological analysis reveals shear-thinning behaviour of the hybrid electrolyte. The complex viscosity (η*) decreases with increasing angular frequency, from approximately 2.27 Pa·s at low frequency (~1 rad/s) to ~0.23 Pa·s at higher

frequencies (~10 rad/s). Notably, the complex viscosity of the MC-WiSE was slightly higher that the 17 m WiSE at low frequency and was almost comparable at higher frequency.

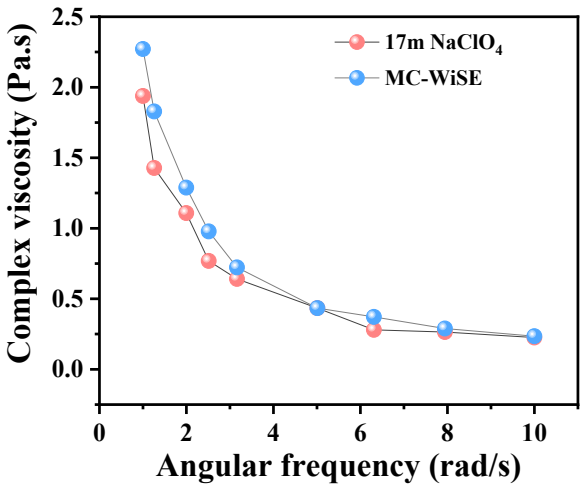


**Figure S3**: Variation of complex viscosity as a function of angular frequency of 17 m $NaClO_4$ and the MC-WiSE

**pH across different temperature:**

The pH of the Mc-WiSE was found to be 6.75 at room temperature, which decreased slightly to 6.2 at an elevated temperature of 60°C.

**Differential scanning calorimetry (DSC):**

Differential scanning calorimetry (DSC) was performed to determine the freezing point of the MC-WiSE, analysis reveals a pronounced freezing point depression, with the crystallization temperature observed at −58.56 °C.

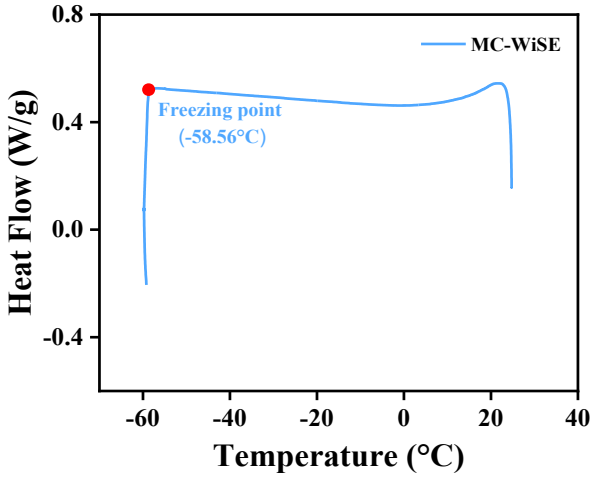


**Figure S4**: DSC profile of the MC-WiSE

**$Na^+$ transport number:**

Uncertainties in transference numbers were estimated using block averaging of molecular dynamics trajectories, wherein transference numbers were calculated independently for each block and the standard deviation was taken as the statistical error. The sodium transference number in the MC-WiSE remains in the range of ~0.28 - 0.35 across 233-333 K, exhibiting weak temperature dependence.

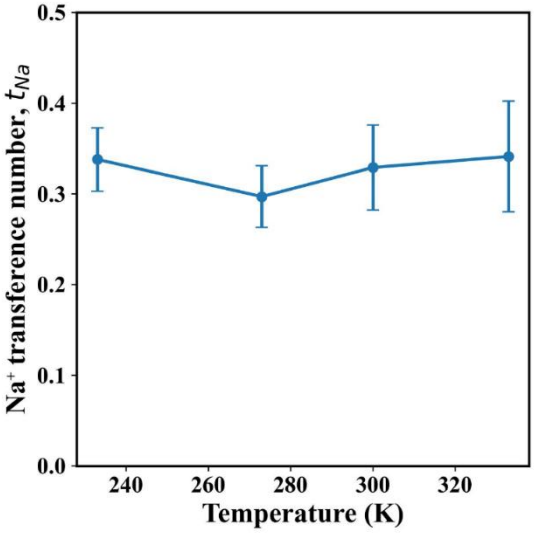


**Figure S5:** Temperature dependence of $Na^+$ transference number in the MC-WiSE

**<u>MD supported quantitative molecular-level analysis of EG's influence on water activity and ion pairing:</u>**

Further the average number of water–water hydrogen bonds in the 17 m $NaClO_4$ in water-EG was quantified employing MD simulation. As EG content increases from 0 to 2.0, the number of water–water hydrogen bonds decrease monotonically (from ~2910 to ~2375), corresponding to an ~18–20 % reduction in the extended water hydrogen-bond network. Since water–water hydrogen bonding underpins network connectivity and electrochemical reactivity of water, this result provides direct quantitative evidence for suppressed effective water activity upon EG incorporation, beyond qualitative spectroscopic interpretation.

The influence of ethylene glycol (EG) on ion–solvent interactions in the MC-WiSE electrolyte is already quantitatively captured in the main manuscript through a combination of radial distribution functions (RDFs), coordination number analysis, and interaction energy calculations, as presented in Figures 3 and 4 and the corresponding discussion sections.

**(i) Disruption of $Na^+$ hydration by EG**

In the baseline aqueous $NaClO_4$ system (Figure 3c–e, main manuscript), sodium ions exhibit a well-defined primary hydration shell dominated by water molecules, with a Na–O($H_2O$) RDF peak at ~0.23 nm and a coordination number decreasing from ~5 to ~3 as salt concentration increases. This already indicates partial dehydration at high molality due to water scarcity.

Upon introducing EG (Figures 3h and 3j, main manuscript), the Na–O ($H_2O$) RDF exhibits a modest increase in first-peak intensity accompanied by reduced integrated coordination, indicating enhanced local ordering but fewer water molecules in the primary $Na^+$ solvation shell rather than stronger hydration. Concurrently, interaction-energy analysis (Figure 3j) reveals a pronounced increase in water–EG and EG–$ClO_4^-$ interactions together with a reduction in water–$NaClO_4$ interaction energy. These combined trends quantitatively demonstrate that EG competes with water for hydrogen bonding, thereby diverting water molecules away from $Na^+$ hydration shells and promoting solvation-structure reorganization.

**Table S1**: Coordination number change of water in first hydration shell of sodium by adding ethylene glycol

| Case | 0 EG | 0.3 EG | 0.8 EG | 1.6 EG | 2.0 EG |
|---|---|---|---|---|---|
| Coordination Number | 2.746 | 2.630 | 2.472 | 2.352 | 2.225 |

**(ii) Promotion of partial ion pairing**

Concurrently, the Na–O($ClO_4^-$) RDF (Figures 3d and 3i, main manuscript) shows increased peak intensity and closer cation–anion proximity with increasing EG content. This trend is fully consistent with the Raman and ATR-FTIR analysis (Figure 2f–g), where the fraction of contact ion pairs (CIP) increases from ~35% in 17 m $NaClO_4$ to ~45.7% in the MC-WiSE electrolyte.

The MD results therefore provide a molecular-level explanation for this spectroscopic observation: by capturing water molecules through EG–water hydrogen bonding, EG reduces the availability of water to maintain solvent-separated ion pairs, thereby promoting partial $Na^+$–$ClO_4^-$ association rather than free-ion solvation.

(iii) **Connection to suppressed water activity and extended ESW**

The water–water hydrogen-bond statistics (**Figure S5**) quantitatively complement these findings by showing a monotonic reduction in the number of water–water hydrogen bonds with increasing EG content, confirming disruption of the percolating hydrogen-bond network. When interpreted together with the existing MD solvation data, a coherent picture emerges:

- Water–water hydrogen bonding decreases → breakdown of the extended water network (suppressed water activity)
- EG–water hydrogen bonding increases → sequestration of water into non-networked states
- $Na^+$–water coordination weakens while $Na^+$–$ClO_4^-$ coordination strengthens → partial ion pairing

This collective reorganization of the solvation environment explains why water electrolysis is kinetically suppressed, as experimentally evidenced by the expanded electrochemical stability window (~2.75 V) in LSV measurements (Figure 2a), without invoking chemical passivation or electrolyte decomposition mechanisms.

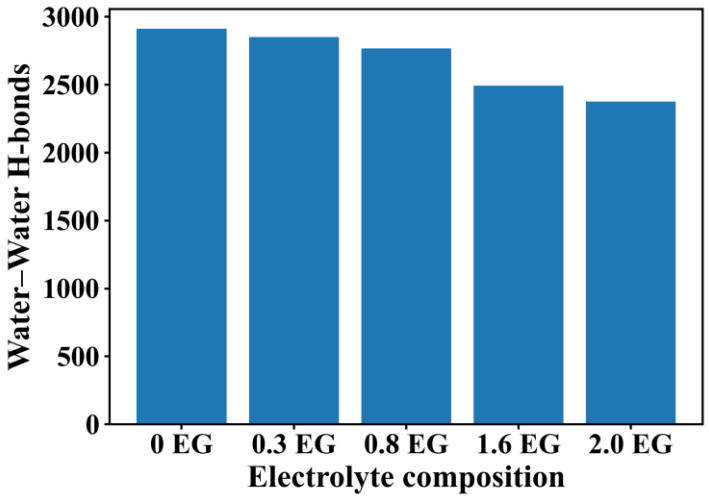


**Figure S6**. Water-water hydrogen bonds the system by the inclusion of ethylene glycol in the system.

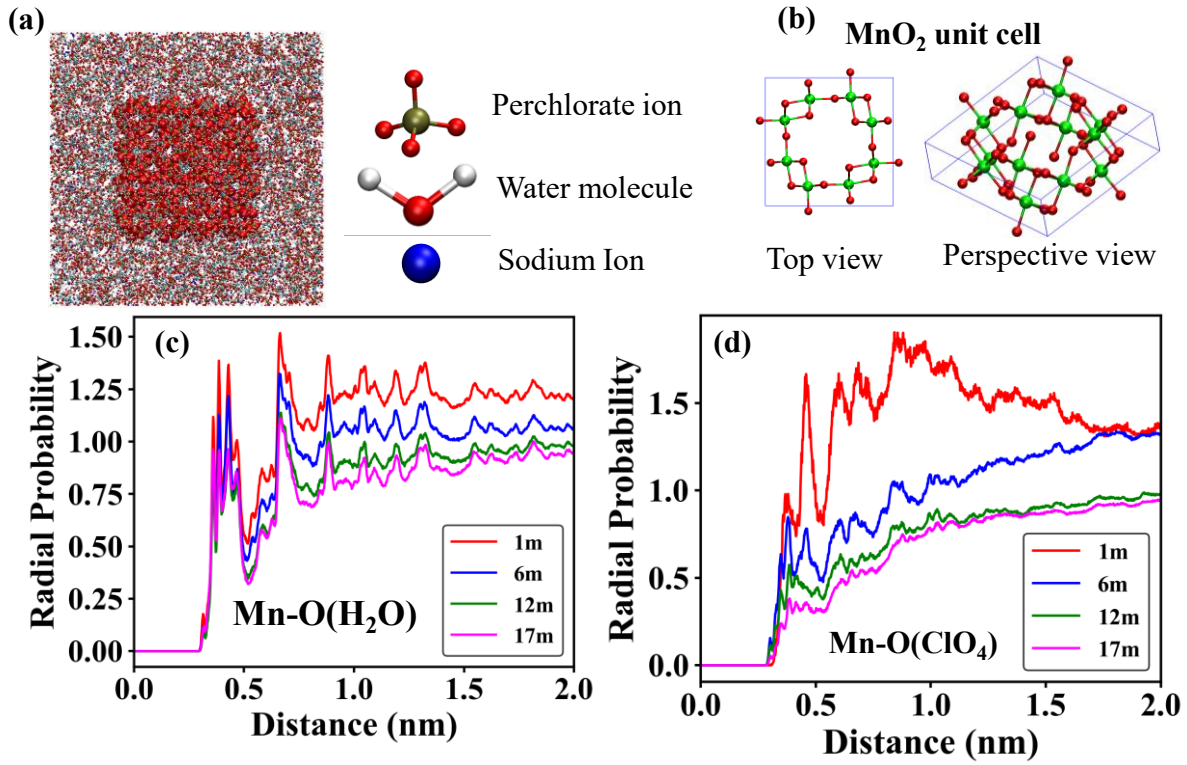


**Figure S7:** Simulation study of electrolyte in presence of electrode material. **(a)** Initial simulation setup and representation of various ions. **(b)** Unit cell representation of electrode material. We use a 4 by 4 array of this unit cell as electrode material. **(c)** Radial density function of oxygen from water molecules from Manganese atoms. **(d)** Radial density function of oxygen from chlorate ions from Manganese atoms.

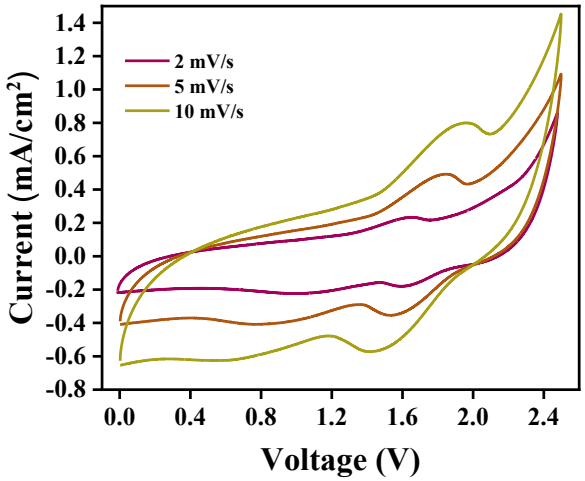


**Figure S8:** CV profile of $MnO_2$-SSC at low scan rates of 2-10 mV/s at room temperature

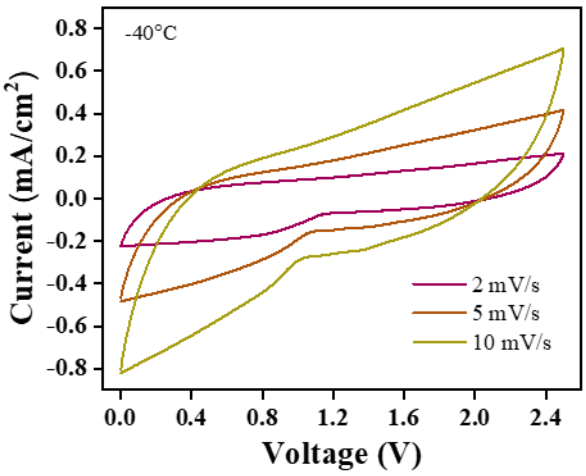


**Figure S9:** CV profile of $MnO_2$-SSC at low scan rates of 2-10 mV/s at -40 ˚C

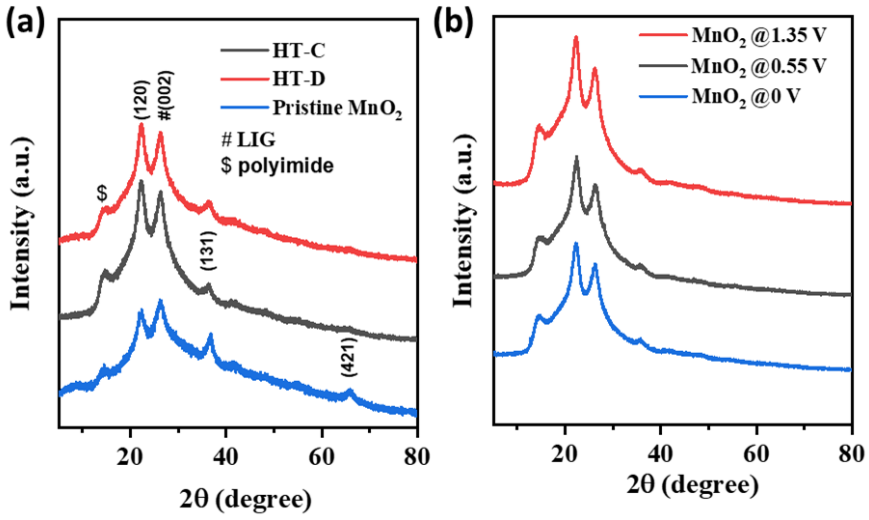


**Figure S10**: Ex-situ XRD pattern (a) of the $MnO_2$ electrode interrupted at fully charged (HT-C) and discharged state (HT-D) while cycling at high temperature (~60˚C) for 1000 cycles, and (b) at different state of discharge during the second cycle.

**Alternating temperature long term cycles of −40 °C→RT→60 °C**

Further we performed long term cycling at alternate temperature, where we continued cycling the cell initially for 3340 cycles at a low temperature of -40°C, followed by 1000 cycles at room temperature followed by 230 cycles at ~60°C (**Figure S11**).

With a starting capacitance of ~8.9 mF/cm$^2$, the cell retained a capacitance of 8.1 mF/cm$^2$ after ~3340 cycles. Upon switching to room temperature, the cell showed an improved starting capacitance of ~26.5 mF/cm$^2$ and retained ~13.8 mF/cm$^2$ after another 1000 cycles. Further when switched to 60°C, the cell showed an increased capacitance of ~79 mF/cm$^2$ and retained a capacitance of ~76 mF/cm$^2$ after 230 cycles.

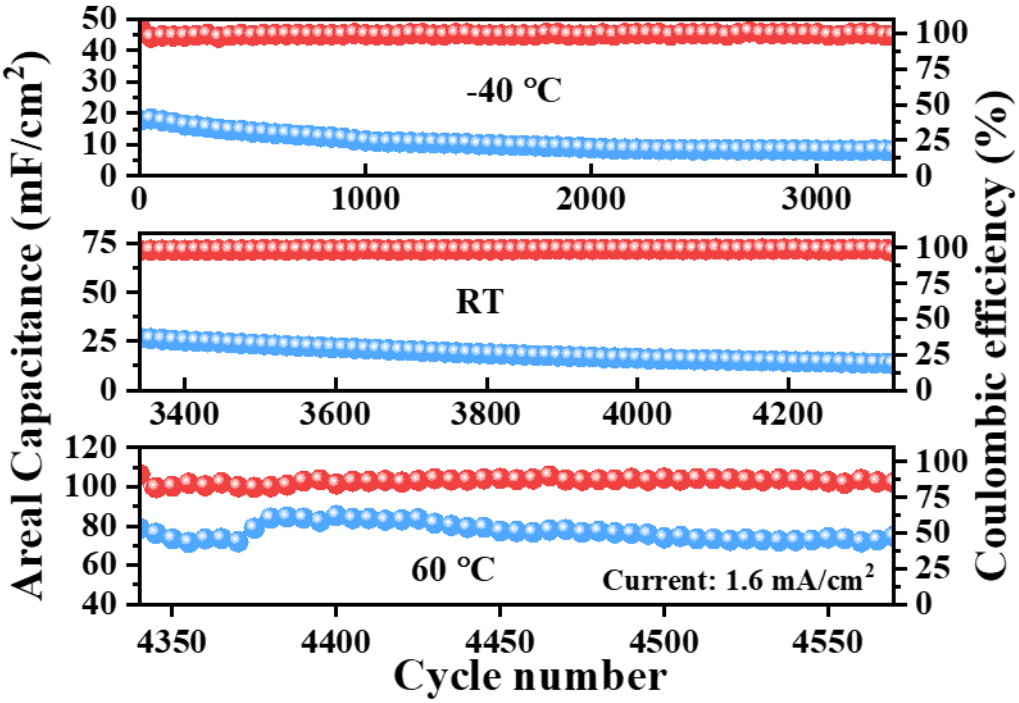


**Figure S11:** Alternating temperature long term cycling at −40 °C (3340 cycles) → RT (1000 cycles) → 60 °C (230 cycles)

**MC-WiSE (Ethylene glycol oxidation) electrochemical stability under the applied potential range and long-term cycling:**

To evaluate possible ethylene glycol (EG) oxidation and electrolyte degradation during prolonged cycling within the operational potential range of 0-2.5 V, $^{1}H$ and $^{13}C$ NMR analyses were performed on the recovered electrolyte after 10,000 cycles at 60 °C, and 1000 cycles at room temperature.

The $^{1}H$ NMR spectra show identical chemical shifts and peak profiles for pristine and cycled electrolytes. No additional resonances are observed that would indicate oxidative degradation products such as glycolaldehyde, glyoxal, or carboxylic acids. The characteristic EG proton signals remain unchanged in position and intensity.

Similarly, the $^{13}C$ NMR spectra exhibit no new carbon related signals and no peak broadening or chemical shift variation. The characteristic EG carbon resonance (~62–65 ppm) remains invariant after cycling at both temperatures.

These results confirm the absence of detectable EG oxidation, even after extended cycling at elevated temperature, demonstrating the excellent chemical and electrochemical stability of the MC-WiSE electrolyte.

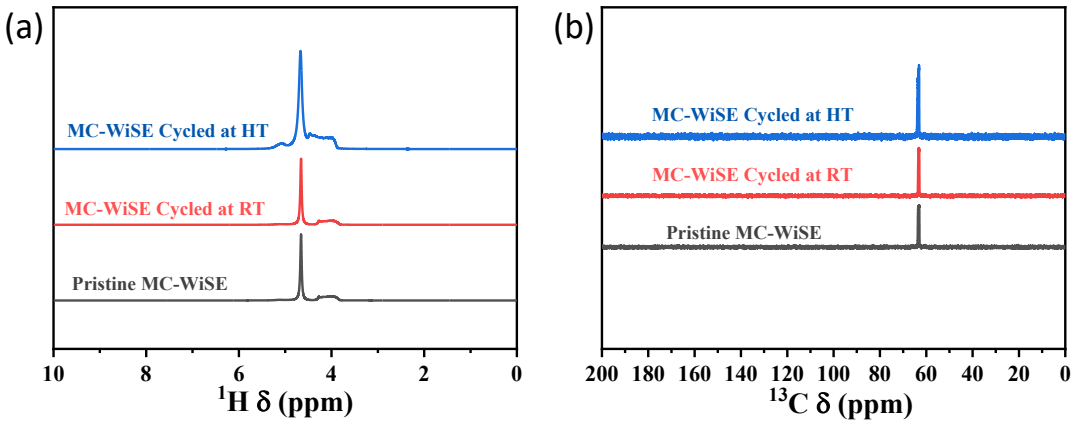


**Figure S12:** a) $^{1}$H and (b) $^{13}$C NMR of the pristine MC-WiSE and recovered from cycled cells

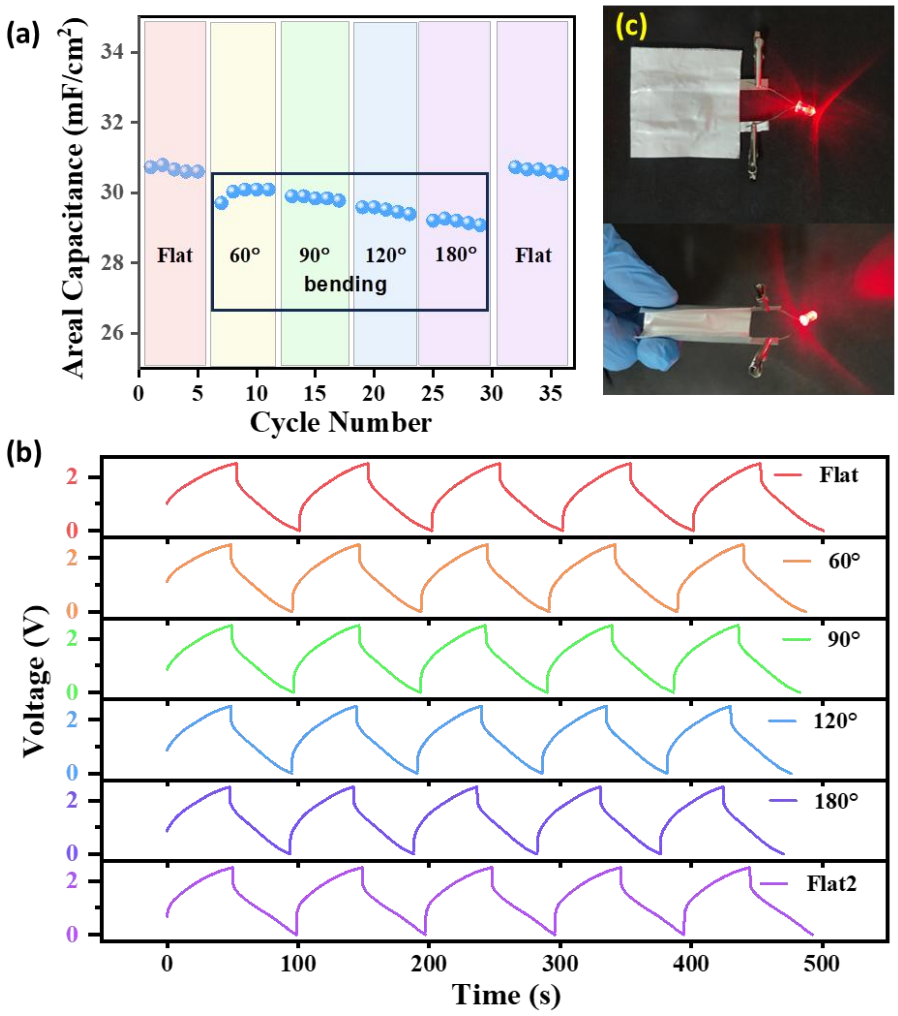


**Figure S13:** Electrochemical performance under flexible conditions: (a) variation of areal capacitance at different bending conditions, (b) GCD profiles obtained at different bending

conditions, (c) digital demonstration of the flexible device powering LED at flat and bending conditions.

**Table S2: Performance comparison table of different supercapacitors at low/high/room temperature with the present work.**

| Sl no | Electrode | Electrolyte | Temperature (˚C) | Potential window (V) | Capacitance at low temp | Cyclic stability | Energy density / Power density | Ref |
|---|---|---|---|---|---|---|---|---|
| **1** | LIG@$MnO_2$ | MC-WiSE | −40°C to 60 °C | 0 to 2.5 V | 25.2 mF/cm$^2$ at 0.32 mA/cm$^2$ –(-40 °C)<br><br>57.8 mF/cm$^2$ at 0.32 mA/cm$^2$ at (RT) | 1.71 mF/cm$^2$ capacitance retention after 4000 cycles (-40 °C)<br><br>5.82 mF/cm$^2$ capacitance retention after 2 lakh cycles (RT) | 21.8 µWh/cm$^2$ at a power density of 396.8 µW/cm$^2$ (-40 °C)<br><br>50.2 µWh/cm$^2$ at a power density of 793.7 µW/cm$^2$ (RT) | **This work** |
| **2** | LIG | PVA/KOH | RT to 80 °C | 0 to 2V | 3.33 mF/cm$^2$ at 0.5 mA/cm$^2$ at RT | 98.7% initial capacitance after 200 cycles at 80 °C | 4.62 µWh/cm$^2$ at 0.5 mA/cm$^2$ at 0.2 mW/cm$^2$ at RT | 4 |
| 3 | rGO | QPPSf-PBI electrolyte | -70 °C to 220 °C | 0 to 1 V | 60 mF/cm$^3$ at 50 mV/s at -70 °C | 81.5% retention at -70 °C at 1 A/g for 5000 cycles | 2.79 mWh/cm$^2$ and 125 mW/cm$^2$ at RT | 5 |
| 4 | PANI/carbon cloth | graphene/PVA organo-hydrogel | -65 °C to 25 °C | | 252 F/g at 1 A/g at -65 °C | 92 % retention at -65 °C | | 6 |
| 5 | N-doped graphene | PAAK/CMC-24 M | −20 °C to 70 ° C | 0 to 2.1 | 55.1 F/g at 0.3 A/g at RT | 97.9% after 10,000 cycles at −20 °C | 33 W h/kg at 311.4 W/kg at RT | 7 |

| | | | | | | | | |
|---|---|---|---|---|---|---|---|---|
| 6 | activated carbon | 4 m LiCl/EG @PAMPS/ PAAm hydrogel | −20 °C to 80 °C | 0 to 1 V | 43 F/g at a current density of 1 A/g at RT | 97.9% after 10,000 cycles at −20 °C | 5.97 Wh/kg and a power density of 999.6 W/kg | 8 |
| 7 | EG-PME-Ppy | EG-PAM/MMT /$EMIMBF_4$ | `-30 °C to 40 °C | 0 to 0.8 V | 80 mF/$cm^2$ at 0.8 mA/$cm^2$ at -30 °C | 92.5% after 1000 cycles at RT | 9.4 μWh/$cm^2$ at power density of 319.5 μW/$cm^2$ at RT | 9 |
| 8 | Graphene@CC //Zn | PVA/ethylene glycol | -40 °C to RT | 0 to 2.4 V | 208.8 F/g at 0.2 A/g at RT | 30,000 cycles at 5 A/g at -20 °C | 137.2 Wh/kg at the power density of 199.7 W/kg at RT | 10 |
| 9 | activated carbon | HPC/PVA hydrogel with $LiClO_4$ water/glycerol | -40 °C to 20 °C | 0 to 1.8 V | 143.6 F/g at 0.2 A/g at -40 °C | 71.05% after 5000 cycles at 2 A/g at -40 °C | 23.3 Wh/kg at a power density of 177.2 W/kg at RT | 11 |
| 10 | graphene | MMT/PVA | −50 °C to 90°C | 0 to 0.8 V | 161 F/g at a current density of 1 A/g at -50 °C | 95% even after 10000 cycles at 1 A/g -50 °C | – | 12 |
| 11 | PANI | PA-Gly-Ca | −20 °C to 60 °C | 0 to 1.2 V | 127 mF/$cm^2$ at 1mA/$cm^2$ at -20 °C | – | – | 13 |
| 12 | PANI@CC | (PAA) (SL-g-PAA-Ni) hydrogel | -20 °C to RT | 0 to 0.9 V | 252 F/g at 20˚C | 96.7% after 3000 cycles 20˚C | 26.97 Wh/kg and power density of 2667 W/kg at −20 °C | 14 |
| 13 | $SiP_2$ | DMSO@LiCl | -30 °C | 0 to 2 V | 12.39 mF/$cm^2$ (10.25 F/g) | 82.37% after 30,000 cycles | 4.5 μWh/$cm^2$ and 90.5 μW/$cm^2$ | 15 |
| 14 | LIG@$V_5O_{12}\cdot 6H_2O$ | 17m $NaClO_4$-WEG | −40°C to 60 °C | 0 to 2.5 V | 129.8 mF/$cm^2$ (740.4 F/g) at 1 A/g at -40 °C | 80,950 cycles with a capacitance of 25.7 mF/$cm^2$ at 10 A/g at RT | 112.6 and 12.5 μWh/$cm^2$ at 436.5 and 4365 μW/$cm^2$ respectively at -40 °C | 16 |

**References**


1. Evans, D. J.; Holian, B. L., The Nose–Hoover thermostat. *The Journal of Chemical Physics* **1985,** *83* (8), 4069-4074.
2. Van Der Spoel, D.; Lindahl, E.; Hess, B.; Groenhof, G.; Mark, A. E.; Berendsen, H. J. C., GROMACS: Fast, flexible, and free. *Journal of Computational Chemistry* **2005,** *26* (16), 1701-1718.
3. Humphrey, W.; Dalke, A.; Schulten, K., VMD: Visual molecular dynamics. *Journal of Molecular Graphics* **1996,** *14* (1), 33-38.
4. Awasthi, H.; Renuka, H.; Srivastava, A. K.; Goel, S., Laser-induced graphene-based flexible interdigital electrode realizing micro supercapacitor sustainable in different temperatures. *Energy Storage* **2022,** *5* (3).
5. Chaichi, A.; Venugopalan, G.; Devireddy, R.; Arges, C.; Gartia, M. R., A Solid-State and Flexible Supercapacitor That Operates across a Wide Temperature Range. *ACS Applied Energy Materials* **2020,** *3* (6), 5693-5704.
6. Zheng, H.; Guan, R.; Liu, Q.; Ou, K.; Li, D.-s.; Fang, J.; Fu, Q.; Sun, Y., A flexible supercapacitor with high capacitance retention at an ultra-low temperature of -65.0°C. *Electrochimica Acta* **2022,** *424*.
7. Deng, Y.; Wang, H.; Zhang, K.; Shao, J.; Qiu, J.; Wu, J.; Wu, Y.; Yan, L., A high-voltage quasi-solid-state flexible supercapacitor with a wide operational temperature range based on a low-cost "water-in-salt" hydrogel electrolyte. *Nanoscale* **2021,** *13* (5), 3010-3018.
8. Li, X.; Lou, D.; Wang, H.; Sun, X.; Li, J.; Liu, Y. N., Flexible Supercapacitor Based on Organohydrogel Electrolyte with Long-Term Anti-Freezing and Anti-Drying Property. *Advanced Functional Materials* **2020,** *30* (52).
9. Hu, Q.; Cui, S.; Sun, K.; Shi, X.; Zhang, M.; Peng, H.; Ma, G., An antifreezing and thermally stable hydrogel electrolyte for high-performance all-in-one flexible supercapacitor. *Journal of Energy Storage* **2022,** *50*.
10. Liu, J.; Khanam, Z.; Ahmed, S.; Wang, T.; Wang, H.; Song, S., Flexible Antifreeze Zn-Ion Hybrid Supercapacitor Based on Gel Electrolyte with Graphene Electrodes. *ACS Applied Materials & Interfaces* **2021,** *13* (14), 16454-16468.
11. Lu, N.; Na, R.; Li, L.; Zhang, C.; Chen, Z.; Zhang, S.; Luan, J.; Wang, G., Rational Design of Antifreezing Organohydrogel Electrolytes for Flexible Supercapacitors. *ACS Applied Energy Materials* **2020,** *3* (2), 1944-1951.
12. Lu, C.; Chen, X., All-Temperature Flexible Supercapacitors Enabled by Antifreezing and Thermally Stable Hydrogel Electrolyte. *Nano Letters* **2020,** *20* (3), 1907-1914.
13. Chen, J.; Yu, Q.; Shi, D.; Yang, Z.; Dong, K.; Kaneko, D.; Dong, W.; Chen, M., Tough and Antifreezing Organohydrogel Electrolyte for Flexible Supercapacitors with Wide Temperature Stability. *ACS Applied Energy Materials* **2021,** *4* (9), 9353-9361.
14. Mondal, A. K.; Xu, D.; Wu, S.; Zou, Q.; Lin, W.; Huang, F.; Ni, Y., Lignin-containing hydrogels with anti-freezing, excellent water retention and super-flexibility for sensor and supercapacitor applications. *International Journal of Biological Macromolecules* **2022,** *214*, 77-90.
15. Chang, Y.; Li, Y.; Cui, P.; Guo, Y.; Xu, Y.; Lou, C.; Zhao, M.; Wang, L.; Hu, Q.; Li, P.; Zhou, A., Anti-freezing, high-voltage, and ultra-stable micro-supercapacitors enabled by phase engineering of 2D SiP2 in LiCl–DMSO electrolyte. *Journal of Materials Chemistry A* **2026**.
16. Thippeswamy, P.; Samanta, K.; Arya, V.; Biswas, D.; Kim, H. S.; Bakli, C.; Jung, H. Y.; Ghosh, D., A 2.5 V In-Plane Flexi-Pseudocapacitor with Unprecedented Energy and Cycling Efficiency for All-Weather Applications. *Small* **2024,** *20* (34).